



Full-field strain evolution and characteristic stress levels of rocks containing a single pre-existing flaw under uniaxial compression

Liwang Liu^{1,2} · Haibo Li^{1,2} · Xiaofeng Li¹ · Renjie Wu^{1,2}

Received: 1 August 2019 / Accepted: 22 February 2020 / Published online: 4 March 2020
© Springer-Verlag GmbH Germany, part of Springer Nature 2020

Abstract

In this study, full-field strain evolution and characteristic stress levels of marble samples containing a single pre-existing flaw were comprehensively studied. The full-field strain was performed by digital image correlation (DIC) method, and the variations of characteristic stress levels with respect to inclination angle were discussed. To compare the experimental results, discrete element method was adopted, and the full-field stress evolution was reproduced to reappraise the localization zones. The results indicate that the presence of pre-existing flaws induces strain localization and degradation of mechanical properties for pre-cracked samples. When the strain localization firstly appeared surrounding pre-existing flaws, the axial stress levels at this moment increase with regard to inclination angle, leading to the increase of peak strength, crack initiation stress, crack damage stress, and normalized crack initiation stress. The normalized crack damage stress obtained by experiments shows flaw independency, and the results were verified by simulation results. Based on the full-field stress evolution, the tensile stress in x direction concentrates around pre-existing flaw and its location moves towards flaw tips with the increase of inclination angle. The compressive stress in y direction around pre-existing flaw is lower than other zones, revealing the upper and bottom surfaces of pre-existing flaw deform to each other. When the numerical models are subjected to same axial loading, the full-field stress around pre-existing flaw decrease as the inclination angle increases, which confirmed the results of full-field strain evolution and elucidated the pre-existing flaw with large inclination angle has less effect on degrading the mechanical properties.

Keywords Pre-existing flaw · Digital image correlation method · Full-field strain evolution · Characteristic stress levels · Discrete element method

Introduction

Rocks containing initial defects at different scales behave various mechanical and deformation properties, which are closely associated with the growth of microcracks. The initiation and propagation of microcracks dominantly lead to the instability and failure of practical rock engineering, e.g., rock burst in deep mining, excavation damage zones in nuclear disposal storage, and slope instability (Brideau et al. 2009; Esterhuizen et al. 2011). Therefore, investigation on the cracking process as well as characteristic stress levels of pre-

cracked samples is significant to understand the failure behavior of rock materials.

Numerous experimental investigations had been conducted to study the cracking processes of pre-cracked samples. Initially, polymethylmethacrylate (PMMA), as a kind of homogeneous materials, was selected to confirm the validity of ideal sliding crack model (Nemat-Nasser and Horii 1982). Then by inserting steel slices into uncured gypsum or cement, the rock-like samples with different pre-existing flaws were prefabricated to study the cracking processes and mechanical properties for rocks (Sagong and Bobet 2002; Feng et al. 2018; Liu et al. 2018). The secondary cracks were more difficult to initiate than wing cracks under uniaxial compression (Park and Bobet 2010), while the initiation position of wing cracks moved to the flaw center or disappeared under high confining stresses (Bobet and Einstein 1998). Moreover, the crack coalescence was mainly caused by secondary cracks under uniaxial compression and was only induced by secondary cracks when samples were subjected to high confining

✉ Xiaofeng Li
xfli@whrsm.ac.cn

¹ State Key Laboratory of Geomechanics and Geotechnical Engineering, Institute of Rock and Soil Mechanics, Chinese Academy of Sciences, Wuhan 430071, China

² University of Chinese Academy of Sciences, Beijing 10049, China

stress (Bobet 2000). Due to the fact that microstructures of rock materials are heterogeneous and the properties of mineral components are different, investigations on rock-like materials with homogeneous microstructure are not enough for understanding failure behaviors of rocks. With the development of technique for sample preparation, prefabricating flaws in rocks was available, and numerous experiments were accordingly conducted to investigate the cracking process of natural geomaterials. (Li et al. 2005) investigated the acoustic emission (AE) characteristics and cracking properties of marble samples containing a single pre-existing flaw, it is found that the cracking properties between marble and rock-like material were considerably different. By utilizing high-speed camera to monitor failure processes, the types of cracks initiated in rock samples containing a single pre-existing flaw were determined (Wong and Einstein 2009; Yang and Jing 2011), and the coalescence processes of rock materials were investigated (Feng et al. 2009; Cheng et al. 2015; Zhang et al. 2019b). Even though numerous investigations had been conducted on cracking processes of pre-cracked samples, the characteristic stress levels representing crack initiation and propagation are not systematically studied.

As an effective full-field and non-contact measurement method, digital image correlation (DIC) method has been utilized in experiments for rock materials (Zhang et al. 2015) and pre-cracked samples (Lin et al. 2019; Yang et al. 2019). The crack initiation and coalescence processes of pre-cracked samples prepared by rock-like materials were analyzed; the full-field strain obtained by DIC was consistent with the processes of crack growth (Zhao et al. 2018, 2019), revealing that the DIC method is useful and efficient to investigate the full-field strain evolution of pre-cracked samples. However, the variations of full-field strain with respect to inclination angle and the relationship between full-field strain and characteristic stress levels of pre-cracked rocks are not well understood.

In the study, marble samples containing a single pre-existing flaw were compressed to failure under uniaxial compression. The mechanical characteristics, particularly characteristic stress levels, were analyzed with regard to inclination angle, and the full-field strain during compression was calculated based on the DIC method. Furthermore, to verify the experimental results, discrete element method (DEM) was adopted for simulation, and the full-field stress was obtained for explaining the strain localization phenomenon.

Sample preparation and experiment methodology

Sample preparation

As presented in Fig. 1c, the dimensions of samples were 50 mm in width, 100 mm in height, and 20 mm in thickness,

respectively. By using the machine of wire-electrode cutting, the pre-existing flaws with seven kinds of inclination angle α varying from 0° to 90° were prefabricated; the width and length of the flaw were 1 mm and 15 mm, respectively. In order to meet the calculation requirements of DIC, the speckles with random gray intensity distributions should cover the samples to deform together with their surfaces (Fig. 1b). To obtain the speckles, the white paint was first sprayed on the sample surfaces uniformly and then the black paint was randomly covered upon them (Zhao et al. 2019).

Experimental equipment

The experimental equipment employed in this study consists of three parts, including rock mechanics test system, acoustic emission (AE) system, and high-speed camera system. As illustrated in Fig. 1a, the axial loads were applied along y direction by rock mechanics test system (MTS 815.04) with 4600 kN maximum axial loading capability; the axial loading velocity was set as 0.0005 mm/s to ensure the samples were in quasi-static condition. Meanwhile, due to the circumferential strain gauge was difficult to be used for prismatic samples, the AE system with six AE sensors (Fig. 1b) was utilized to determine crack initiation stress σ_{ci} . The threshold level for triggering AE recording was set as 45 dB to eliminate the influence of background noise. The test of pencil-lead breaking was employed to ensure the sensors had good contact with samples, and the two sides of samples were treated by petroleum jelly to eliminate end-friction effect. In order to capture the deformation images of sample surfaces for following DIC analysis, the high-speed camera system including a charge-coupled device (CCD) camera, light source, and image acquisition computer was employed. The light source was configured in front of samples to improve the quality of images. The sampling rate of CCD camera is 50 frames per second, and the resolution is 1624×1236 pixels.

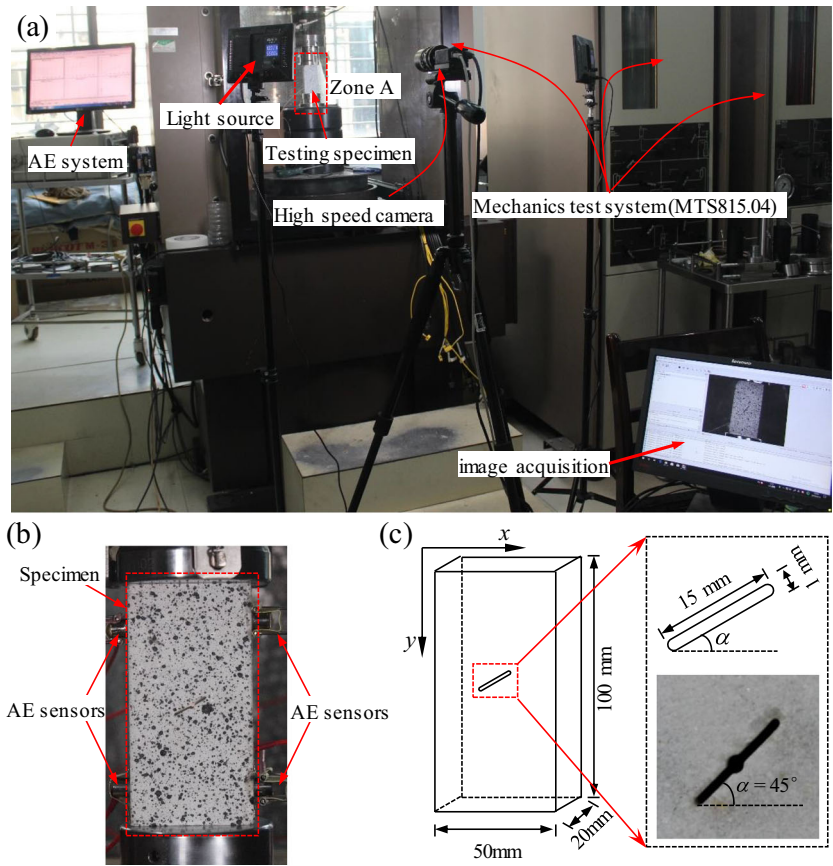
Digital image correlation method

To obtain the full-field strain during experiment, an open source DIC software (Ncorr) was utilized (Blaber et al. 2015). By uninterruptedly tracking and matching the same subset of two images captured before and after deformation, the displacement and strain can be calculated. As shown in Fig. 2, given that there are $(2N + 1) \times (2N + 1)$ pixels in the subset of which center is represented by point $P(x_0, y_0)$, the point $Q(x_i, y_i)$ represents a random pixel, and its displacement can be calculated by following the equations (Blaber et al. 2015),

$$x_i - x_i' = u_0 + \frac{\partial u}{\partial x}(x_i - x_0) + \frac{\partial u}{\partial y}(y_i - y_0) \quad (1)$$

$$y_i - y_i' = v_0 + \frac{\partial v}{\partial x}(x_i - x_0) + \frac{\partial v}{\partial y}(y_i - y_0) \quad (2)$$

Fig. 1 Experimental equipment and sample dimension. **a** Experimental equipment. **b** Zoom-in view of zone A. **c** Sample dimension



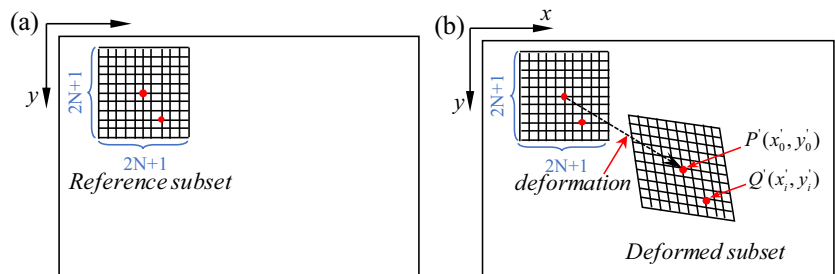
where the symbols $\frac{\partial u}{\partial x}$, $\frac{\partial u}{\partial y}$, $\frac{\partial v}{\partial x}$, and $\frac{\partial v}{\partial y}$ are the first-order displacement gradients of the reference subset; u_0 and v_0 are the displacement components of the reference subset center along x and y direction.

After getting displacements, the corresponding strain components in x and y directions are calculated as follows (Blaber et al. 2015),

$$\epsilon_{xx} = \frac{1}{2} \left[2 \frac{\partial u}{\partial x} + \left(\frac{\partial u}{\partial x} \right)^2 + \left(\frac{\partial v}{\partial x} \right)^2 \right] \quad (3)$$

$$\epsilon_{yy} = \frac{1}{2} \left[2 \frac{\partial v}{\partial y} + \left(\frac{\partial u}{\partial y} \right)^2 + \left(\frac{\partial v}{\partial y} \right)^2 \right] \quad (4)$$

Fig. 2 Schematic illustration for calculation principle of the DIC method. **a** Reference image before deformation. **b** Current image after deformation (modified after Pan et al. (2009))



Experimental results

Mechanical characteristics

After the samples were compressed to failure, the curves of stress versus strain are plotted in Fig. 3a. The peak strength and peak strain of intact sample are 113.4 MPa and 0.52%, respectively. The pre-existing flaw can to some extent degrade the mechanical properties of intact sample. As presented in Fig. 3b, the peak strength and strain of pre-cracked samples as well as their normalized values generally become larger when the inclination angle increases; the variation ranges of peak strength and strain are 72.5~113.0 MPa and 0.40~0.51%, respectively. When the inclination angle approaches 90°, the

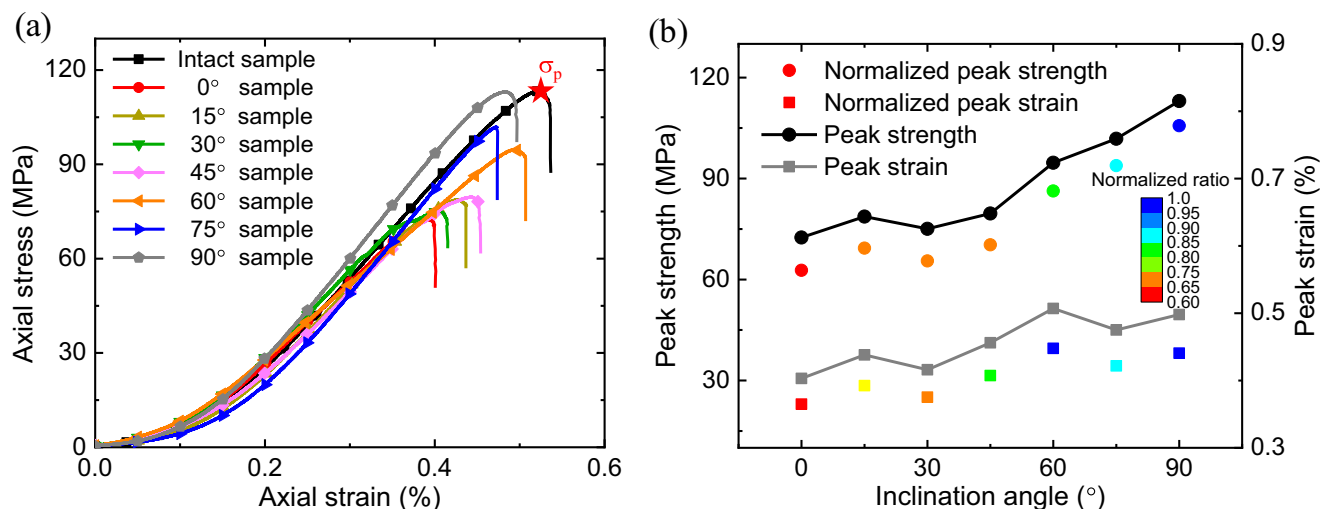


Fig. 3 Mechanical characteristics of pre-cracked samples, **a** stress-strain curves, **b** peak strength, strain, and their normalized values as a function of inclination angle (peak strength and strain of pre-cracked samples are normalized by the corresponding values of intact samples)

normalized peak strength and strain are close to 1. Furthermore, similar to the findings of Liu et al. (2015), the pre-existing flaws with different inclination angles have diverse impacts on mechanical characteristics. As the inclination angle increases from 0° to 90°, the mechanical characteristics of pre-cracked samples first change without obvious variations and then increase dramatically.

Crack initiation and damage stress levels

The failure process of rock under compression can be divided into five stages: (I) crack closure; (II) elastic deformation; (III) crack initiation and stable crack growth; (IV) crack damage and unstable crack growth; (V) failure and post-peak behavior (Brace et al. 1966; Bieniawski 1967; Martin and Chandler 1994; Eberhardt et al. 1998). At the onset of loading, the stress-strain curve behaves non-linear in the stage I, and the axial stiffness increases progressively. When the axial stiffness almost stays unchangeable, the rock enters stage II and the corresponding stress level is defined as crack closure stress σ_{cc} . At the end of stage II, the initiation and propagation of microcracks occur in rocks in a stable manner; the stress level is defined as crack initiation stress σ_{ci} , which usually represents the in situ spalling strength (Nicksiar and Martin 2012). In addition, during the stage IV, the microcracks propagate and coalesce in an unstable manner; the stress level in the beginning of stage IV is crack damage stress σ_{cd} , which represents the onset of true yield (Diederichs et al. 2004). Therefore, the crack initiation and damage stresses are of importance to estimate the cracking processes of microcracks in rocks.

To date, many methods have been utilized to determine characteristic stress levels for intact rocks, including crack volumetric strain method (CVSM), radial strain method

(RSM), axial stiffness method (ASM), and acoustic emission method (AEM) (Eberhardt et al. 1998; Diederichs et al. 2004; Zhao et al. 2013, 2015a, b; Amann et al. 2014; Moradian et al. 2016; Zhang et al. 2019a, 2020). Based on the results summarized from 953 tests, Li et al. (2020) overviewed the characteristic stress levels of intact rocks and indicated that normalized crack initiation stress is about 0.48 and normalized crack damage stress is about 0.79. In contrast, the investigations on characteristic stress levels of pre-cracked samples are scarce. Previously, the crack initiation stress σ_{ci} was usually obtained by direct observation method (DOM). Once the macroscopic cracks observed directly by naked eyes initiate from pre-existing flaw, the corresponding axial stress level is regarded as crack initiation stress σ_{ci} (Wong and Einstein 2006; Zhuang et al. 2014; Miao et al. 2018; Zhao et al. 2018). Based on previous experimental results under uniaxial compression, normalized crack initiation stress of samples containing a single pre-existing flaw with different inclination angles is summarized in Table 1. Even though normalized crack initiation stress of gypsum or rock-like material seems to present increasing tendency as the inclined angle increases, not all macroscopic cracks can be observed in rock materials before peak strength (e.g., marble and sandstone), thus using DOM to determine the crack initiation stress σ_{ci} of pre-cracked rocks may be not efficient.

To overcome above problems, this study used AEM adopted by Eberhardt et al. (1998) and Amann et al. (2014) to determine crack initiation stress σ_{ci} and ASM adopted by Diederichs et al. (2004) and Diederichs (2007) to identify the crack damage stress σ_{cd} . As illustrated in Fig. 4, the stress level corresponding to the turning point where AE counts increase obviously is regarded as the onset of crack initiation, namely crack initiation stress σ_{ci} . The crack initiation stress of 0°, 30°, 60°, and 90° samples are 36.0 MPa, 36.8 MPa,

Table 1 Normalized crack initiation stress of different samples containing a single pre-existing flaw under uniaxial compression experiments

Sample material	Normalized crack initiation stress σ_{ci}/σ_p (%)							Flaw length (mm)	Flaw width (mm)	Flaw condition	Reference
	0°	15°	30°	45°	60°	75°	90°				
Marble	74.34	—	94.94	98.16	—	—	—	15	1	Open	This study
Sandstone	56.15	59.50	76.50	82.30	87.43	99.19*	89.50*	2	2	Open	Miao et al. (2018)
Gypsum	~80.92	—	~80.92	~92.93	~99.65	—	—	12.5	1.27	Open	Wong and Einstein (2006)
Rock-like material	—	~85.53	~84.53	~85.91	~93.08	~94.97	—	15	1	Open	Zhuang et al. (2014)
Gypsum	—	~77.18	~83.3	~83.06	~66.9	~89.7	—	14	—	Almost close	Zhao et al. (2019)
Gypsum	~46.29	~70.0	~79.5	~90.5	~96.5	~100	—	12.5	0.1	Almost close	Wong and Einstein (2006)
Sandstone	87.00	80.80	86.25	88.03	89.00	82.00*	99.28*	25	2	Gypsum filling	Miao et al. (2018)
Sandstone	73.53*	92.70*	69.20	75.39	95.54	96.80	96.76*	25	2	Cement filling	Miao et al. (2018)
Sandstone	78.79*	91.10*	88.74*	50.65*	45.91*	72.68*	37.77*	25	2	Resin filling	Miao et al. (2018)
Rock-like material	—	~77.61	~79.25	~82.01	~84.91	~86.41	—	15	1	Gypsum filling	Zhuang et al. (2014)

“*” indicates macroscopic cracks occur in the post-peak stage; “—” indicates no macroscopic cracks occur before failure; “~” indicates approximate values obtained from relevant curves

63.1 MPa, and 80.6 MPa, respectively. For crack damage stress σ_{cd} , the axial stress level where axial stiffness decreases is regarded as σ_{cd} , and the crack damage stress of 0°, 30°, 60° and 90° samples are 56.7 MPa, 63.6 MPa, 80.9 MPa, and

95.4 MPa, respectively. By utilizing the same method, the characteristic stress levels of other samples with different inclination angles are determined, and the results are summarized in Table 2.

Fig. 4 Determination of characteristic stress levels by AEM and ASM. **a** 0° sample. **b** 30° sample. **c** 60° sample. **d** 90° sample

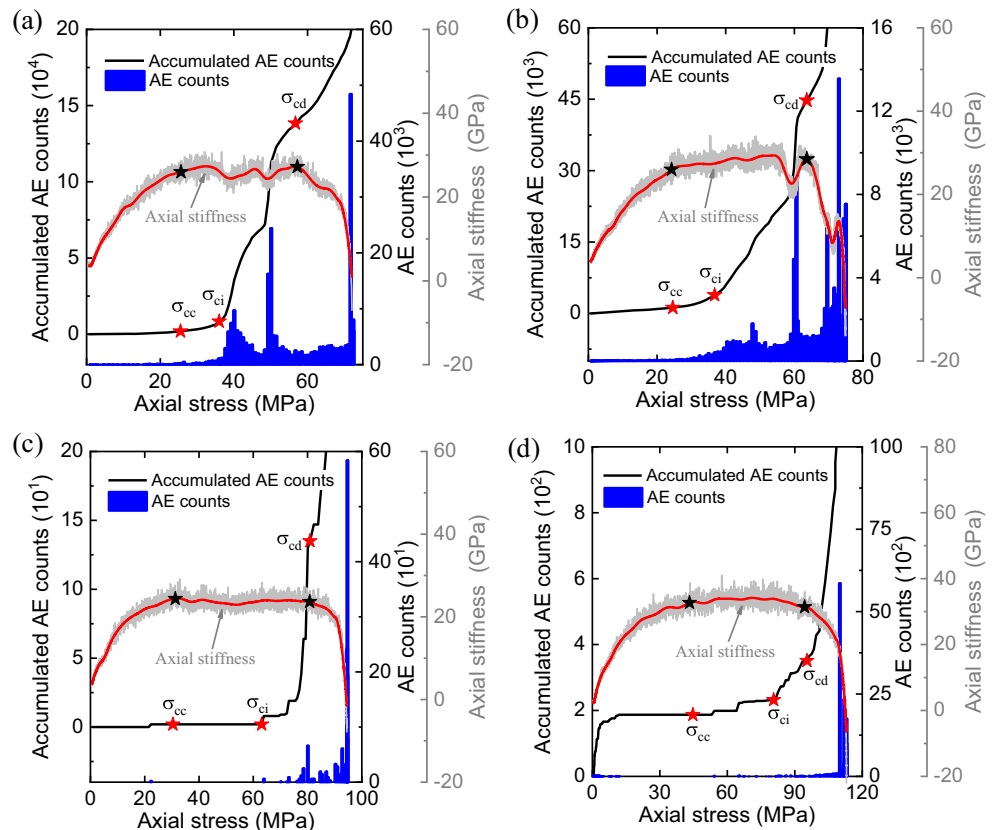


Table 2 Characteristic stress levels obtained in this study

Angle (°)	σ_{cc} (MPa)	σ_{ci} (MPa)	σ_{cd} (MPa)	σ_p (MPa)	σ_{ci}/σ_p	σ_{cd}/σ_p
0	25.5	36.0	56.7	72.5	0.497	0.782
15	28.0	35.3	57.8	78.7	0.449	0.734
30	24.6	36.8	63.6	75.2	0.489	0.846
45	29.3	44.7	60.8	79.6	0.562	0.764
60	30.4	63.1	80.9	94.7	0.666	0.854
75	39.2	74.5	85.3	102.0	0.730	0.836
90	44.7	80.6	95.4	113.0	0.713	0.844

σ_{cc} , σ_{ci} , and σ_{cd} represent crack closure stress, crack initiation stress, and crack damage stress, respectively. σ_p represents peak strength. σ_{ci}/σ_p and σ_{cd}/σ_p are crack initiation stress and damage stress normalized by peak strength

The variations of characteristic stress levels are plotted in Fig. 5; the crack initiation and damage stresses exhibit increasing tendencies with the increase of inclination angle. When the inclination angle is small, the crack initiation and damage stresses change slowly, while these stresses increase dramatically when the inclination angle is large (Fig. 5a). In addition, the normalized crack initiation stress generally behaves in an increasing trend (Fig. 5b), revealing the microcracks with large inclination angle are more difficult to initiate than these with small inclination angle. Compared with the results of gypsum or rock-like material in literatures (Wong and Einstein 2006; Zhuang et al. 2014; Miao et al. 2018; Zhao et al. 2018), the normalized crack initiation stress obtained by DOM generally increases and agrees well with the results obtained in this experiment. However, the normalized crack initiation stress obtained by DOM is higher than that obtained by acoustic emission method (Fig. 5b), because AE technique can detect the microscopic fracture prior to macroscopic fracture. In terms of crack damage stress, though the stress increases as the inclination angle increases, its normalized stress fluctuates around a constant (~ 0.8).

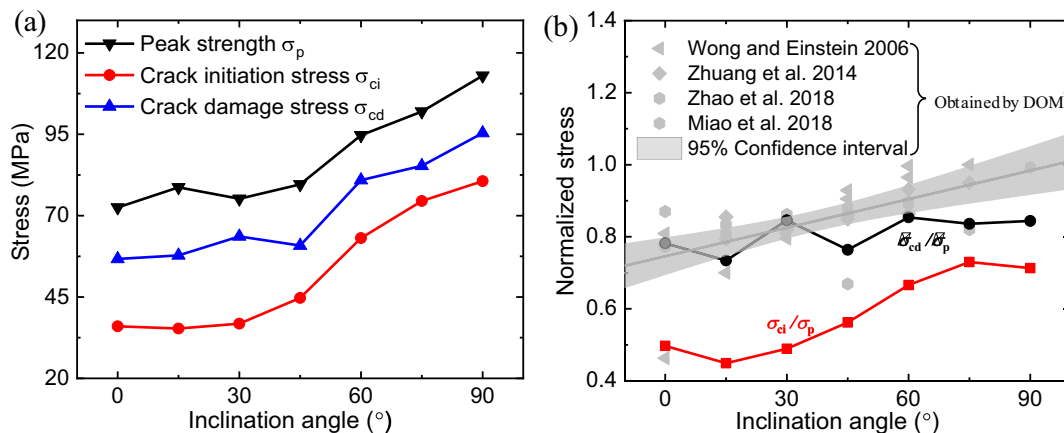


Fig. 5 Characteristic stress levels with regard to inclination angle. **a** Crack initiation and damage stresses. **b** Normalized crack initiation and damage stresses

Full-field strain evolution

To obtain the full-field strain evolution during experiments, the photos captured from the onset to the end of experiments were analyzed based on the DIC method. As illustrated in Fig. 6, the full-field strain evolution processes of pre-cracked samples with 0°, 15°, and 30° inclination angle are illustrated. For 0° and 15° samples (Fig. 6a, b), the strain in x direction appeared localization phenomenon at stage B and the strain localization (SL) zones I and II symmetrically concentrated around the center of pre-existing flaw. When the axial stress increases into stage D, the SL zones III, IV, and V occurred in 0° sample, and the SL zones III and IV appeared in 15° sample, resulting in the evolution of the SL zone II formed previously was constrained. Therefore, the SL zones chronologically formed around pre-existing flaw can interact with each other, and the damage or fracture processes of pre-cracked samples are complicated. As the axial stress increases to peak strength, more SL zones formed and four obvious SL zones were distributed around pre-existing flaws. In comparison, the strain evolution process of 30° sample during stage A to stage D was similar with 0° and 15° samples, while only two obvious SL zones were distributed around pre-existing flaw when sample failed.

Figure 7 is the full-field strain evolution of pre-cracked samples with 45°, 75°, and 90° inclination angle. In contrast with above samples, the strain evolution process of 45° sample was similar to 30° sample, and two obvious SL zones appeared around pre-existing flaw when axial loading approaches its peak strength (Fig. 7a). However, the 75° and 90° samples have different strain evolution processes; the SL zones are difficult to form at the onset of axial loading (i.e., stage A to D in Fig. 7b, c). When the sample approaches failure, the SL zones suddenly formed and sample failed violently.

Based on above analysis, the variations of characteristic stress levels with regard to inclination angle have some relationship with the full-field strain evolution. Obviously, the

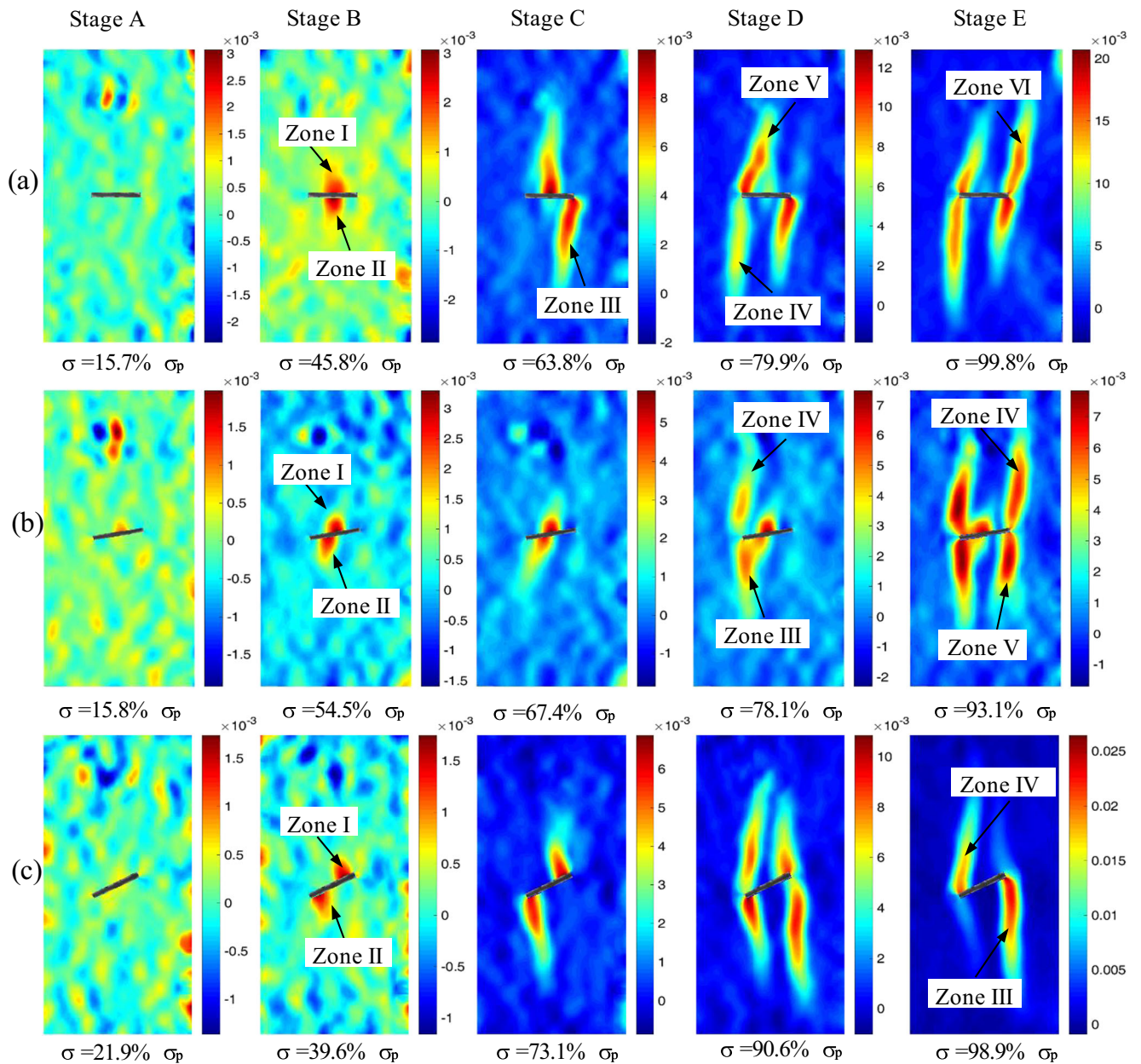


Fig. 6 Full-field strain evolution of pre-cracked samples with different inclination angles. **a** 0° sample. **b** 15° sample. **c** 30° sample

width of pre-existing flaws fabricated artificially is not small enough, which results in the upper and bottom surfaces deform to each other (Fig. 8a). Accordingly, the SL zones representing the crack initiation firstly form around the flaw center. Then the SL zones occur in the tips of pre-existing flaw, which is same to the ideal sliding crack (Fig. 8b) modeled by Horii and Nemat-Nasser (1985). As illustrated in Fig. 8c, when the SL zones firstly form around pre-existing flaw, the axial stress levels at this moment are different in terms of inclination angle. As for pre-cracked samples with small inclination angle, the variations of axial stress levels where SL zones first appear change slightly. With the increase of inclination angle, the SL zones are difficult to form

for the first time. Therefore, the upper and bottom surfaces of pre-existing flaws with large inclination angle are hard to deform to each other, which can explain why mechanical characteristics, namely peak strength, crack initiation, and damage stresses, increase with respect to inclination angle.

DEM simulation and results

DEM proposed by Cundall and Strack (1979) is an effective method to simulate the mechanical characteristics and cracking processes of rock materials (Potyondy and Cundall 2004; Cho et al. 2007; Li et al. 2018a, 2019). During the last few decades,

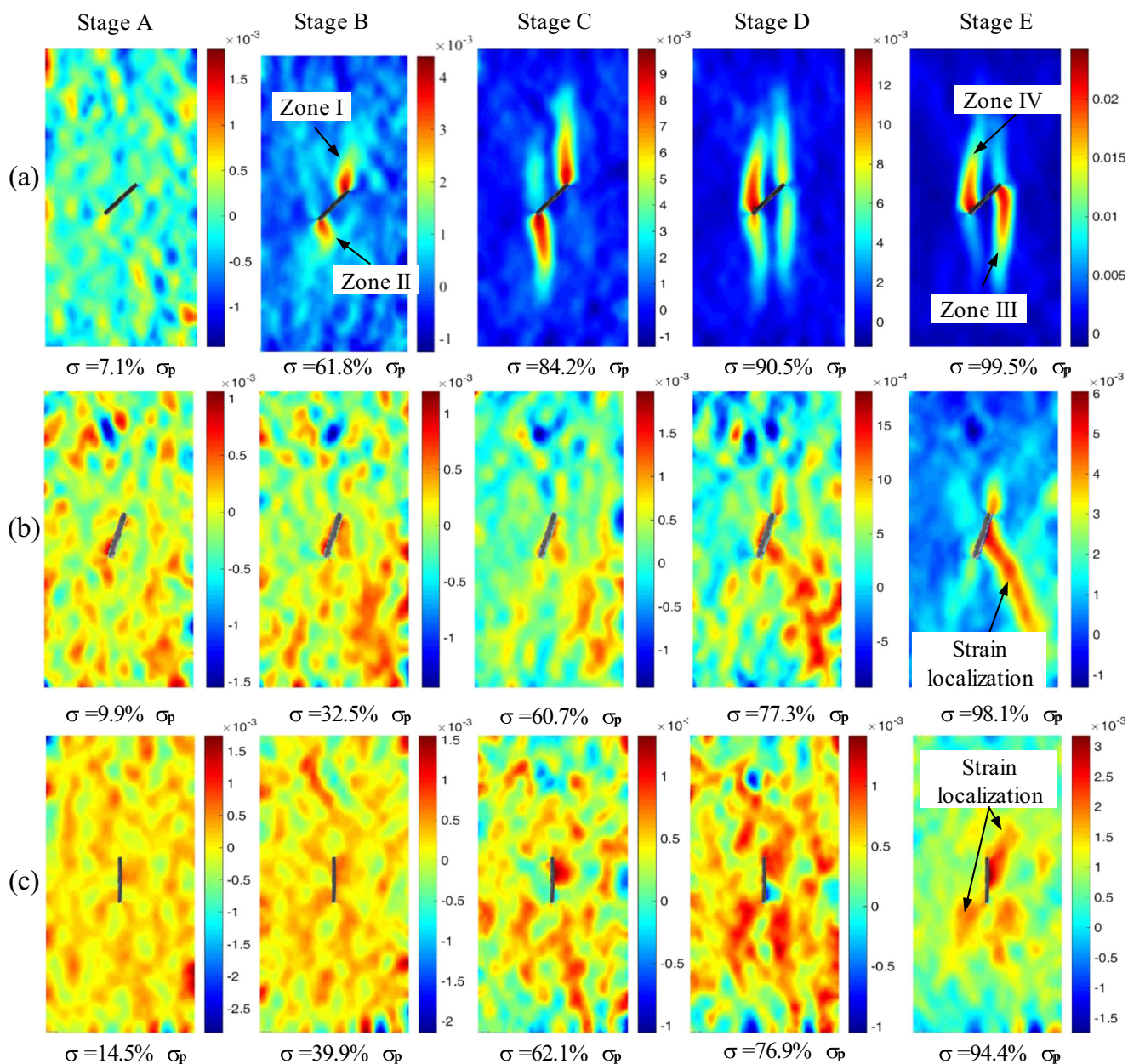


Fig. 7 Full-field strain evolution of pre-cracked samples with different inclination angles. **a** 45° sample. **b** 75° sample. **c** 90° sample

the behaviors of pre-cracked samples under compression had been studied based on this method (Liu et al. 2016; Lee et al. 2017). By taking advantage of particle flow code (PFC), the cracking processes of rock-like materials containing a single pre-existing flaw were simulated (Zhang and Wong 2012); the mechanical characteristics and coalescence behavior of cracks generated in red sandstone with two parallel pre-existing flaws were investigated (Yang et al. 2014). Furthermore, as the cracks initiate and propagate in pre-cracked samples, the full-field displacements were obtained and illustrated for better understanding the fracturing processes (Jin et al. 2017). Accordingly, the discrete element method was selected in this study to verify and explain the experimental results.

Model generation and parameter calibration

In this work, PFC was utilized to mimic the rock samples containing a single pre-existing flaw. The rectangular numerical models with 50 mm in width and 100 mm in height were assembled by 35,082 rigid particles of which radii vary from 0.3 to 0.498 mm and follow uniform distribution (Fig. 9a). To generate the pre-cracked models, the area owning same geometric size with pre-existing flaw (1 mm in width and 15 mm in length) was defined, and then the particles among it were deleted from intact sample (Fig. 9a). In this study, the contact model for gluing these particles is parallel bond model (PBM), which

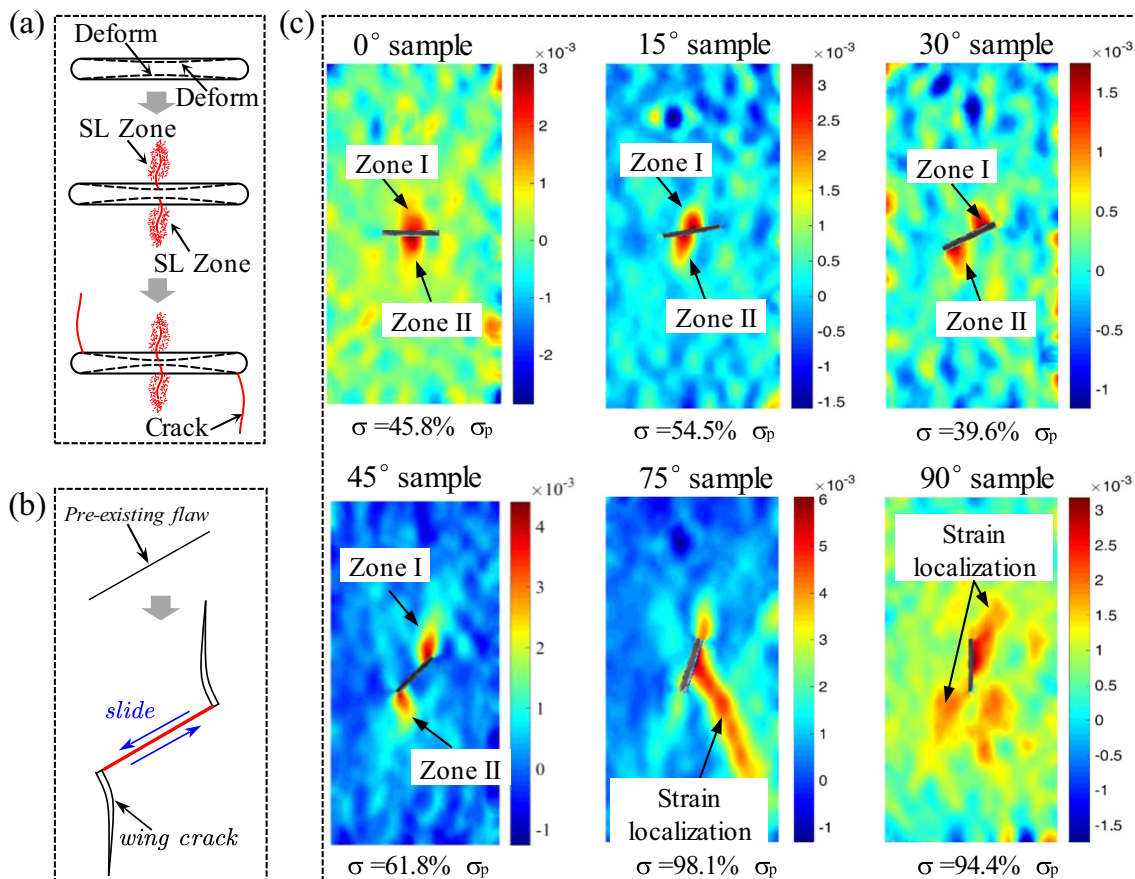


Fig. 8 Schematics of crack evolutions and the full-field strain distributions of samples at the onset of axial loading. **a** Schematic of crack evolution (SL is the abbreviation of strain localization). **b** Schematic

evolution process of ideal sliding crack (modified after Horii and Nemat-Nasser (1985)). **c** Full-field strain distributions of samples at the onset of axial loading

can be envisaged as a set of elastic springs uniformly located over a rectangular area between two adjacent particles (Cho et al. 2007; Zhang and Wong 2012; Zhang et al. 2016). By setting micro-parameters to follow Gaussian distributions, the heterogeneity of rock materials can be better mimicked (Diederichs et al. 2004). According to Newton's second law and force-displacement law, the set of elastic springs would deform during simulations. As illustrated in Fig. 9b, when the adjacent particles move away from each other along the normal direction and the stress applied between them exceeds the tensile strength, the normal spring breaks and tension crack forms. On the other hand, the shear crack forms when the adjacent particles move away from each other along the tangential direction and the stress exceeds shear strength. When the microcracks cluster and coalesce to some extent, the DEM model fails and macroscopic fracture surfaces occur. Moreover, in order to accurately model the loading condition in experiments, the upper loading platen in DEM simulation was fixed, and the compressive stress was applied by moving bottom loading platen at a constant velocity (Fig. 9a).

In DEM simulation, the micro-parameters are difficult to determine by conducting laboratory experiments due to their ambiguous relationship; thus, parameter calibration is an essential step before simulation and is usually based on "trial and error" method adopted by Lee and Jeon (2011), Zhang and Wong (2012), and Li et al. (2016). In terms of the simulation of pre-cracked samples, when the peak strength of intact and pre-cracked samples in simulation agrees well with the experimental results, the variations of characteristic stress levels would be more convincing. Therefore, based on the calibration processes of Jin et al. (2017), the mechanical properties of intact sample were firstly calibrated in this study and then the pre-cracked samples with same micro-parameters were simulated. If the peak strength of pre-cracked samples in simulation did not agree well with the experimental results, the micro-parameters would be changed and the models were simulated again. After numerous tests of simulation, the micro-parameters that have good effects for simulation are shown in Table 3, and the comparison of mechanical properties between experiment and simulation is presented in Fig. 10. The

Fig. 9 DEM models and principles of PBM. **a** DEM models. **b** Principles of PBM (modified after Cho et al. (2007), Li et al. (2018a, b), and Wu et al. (2020))

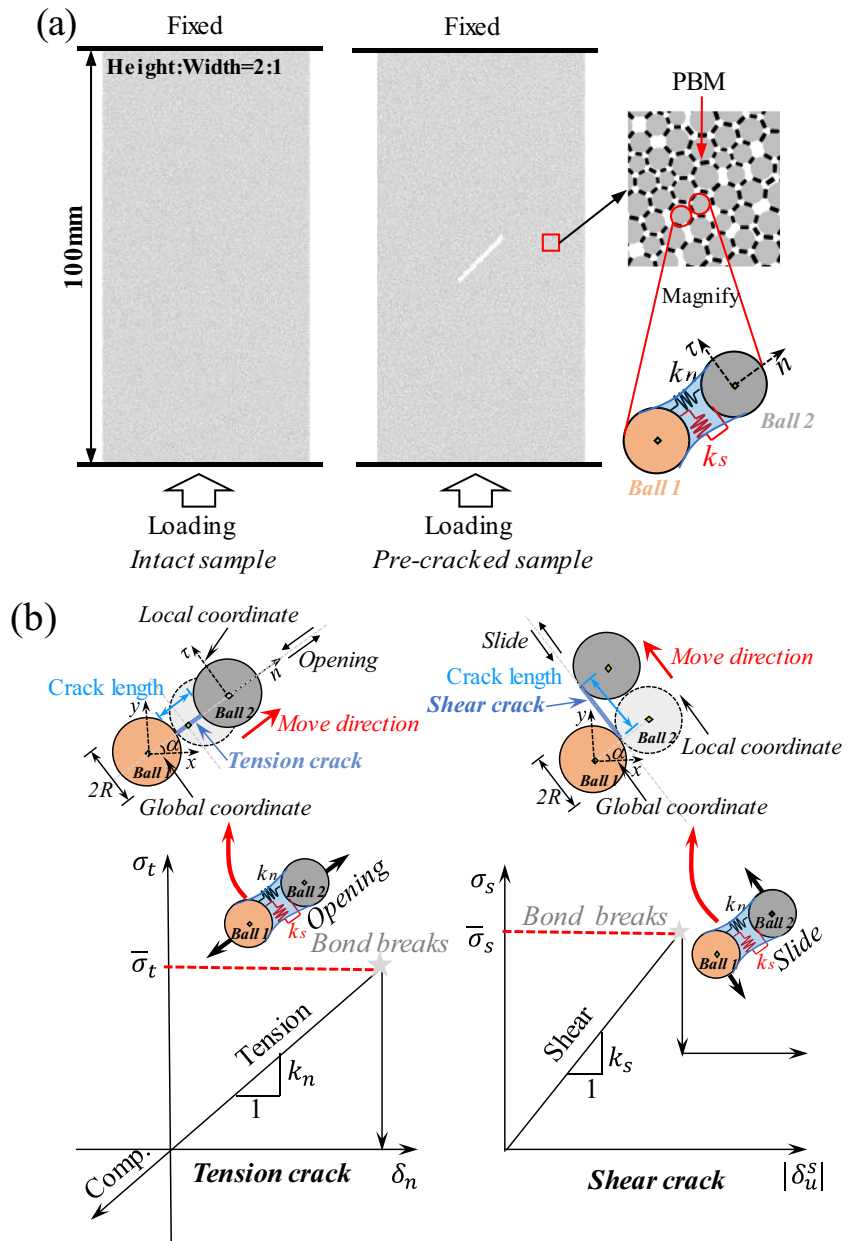


Table 3 Micro-parameters adopted in DEM simulation

Micro-parameters	Values
Minimum particle radius R_{min}	0.3 (mm)
Particle radius ratio R_{max}/R_{min}	1.66
Particle elastic modulus E_b	14.5 (GPa)
Particle stiffness ratio k_n/k_s	1.7
Parallel bond elastic modulus E_P	14.5 (GPa)
Parallel bond elastic modulus \bar{k}_n/\bar{k}_s	1.7
Friction coefficient μ	0.76
Tensile strength (ave \pm std.dev)	29.8 \pm 2 (MPa)
Shear strength (ave \pm std.dev)	45.8 \pm 2 (MPa)

The symbol ave represents average value; the symbol std.dev represents standard deviation

peak strength and elastic modulus obtained by DEM simulation are 114.6 MPa and 30.8GPa, respectively, which are in good consistent with the experimental results (the peak strength is 113.3 MPa and the elastic modulus is 31.0 GPa). The microcracks induced by the breakage of PBM are mainly consisted of tensile cracks (Fig. 10a), which accords with the results of SEM observation conducted by Tapponnier and Brace (1976) and Kranz (1979). In addition, the peak strength and elastic modulus of pre-cracked samples obtained by DEM simulations generally increase with respect to inclination angle and do not have great difference with the experimental results, revealing the parameters calibrated are effective and can be used for following analysis.

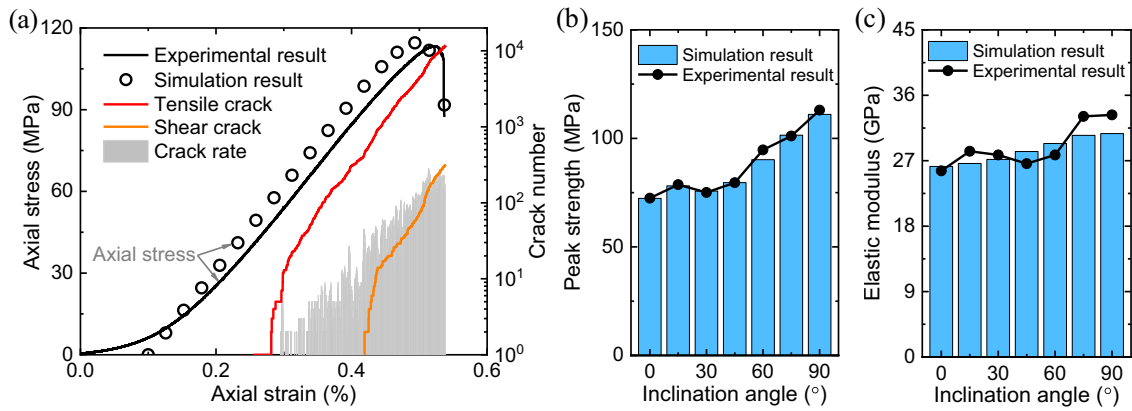


Fig. 10 Comparison of mechanical properties between experiment and simulation. **a** Mechanical properties of intact sample obtained by experiment and simulation (curve of axial stress obtained by simulation

is transformed along x axis for better comparison). **b** Peak strength of pre-cracked samples obtained by experiments and simulations. **c** Elastic modulus of pre-cracked samples obtained by experiments and simulations

Crack initiation and damage stress levels

To verify the experimental results of characteristic stress levels, the crack initiation and damage stresses of DEM models with different inclination angles are determined for comparison. Based on previous studies, there are many methods adopted for determining crack initiation

stress in DEM simulation, such as direct observation method (Zhang and Wong 2012), crack number ratio method (Jin et al. 2017), and Poisson ratio method (Diederichs et al. 2004; Diederichs 2007). In direct observation method, crack initiation stress is considered as the axial stress level where the first microcrack is observable (Zhang and Wong 2012). In crack number

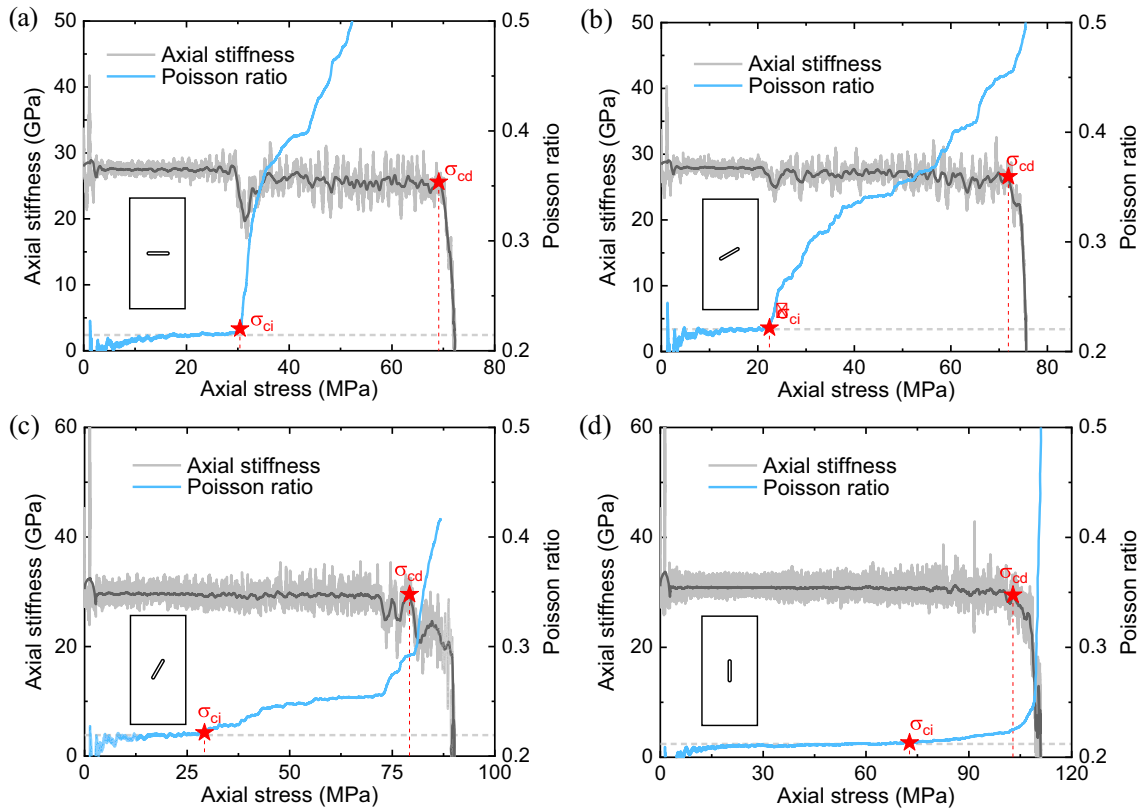


Fig. 11 Determination on crack initiation and damage stresses of pre-cracked samples by using the Poisson ratio method and ASM. **a** 0° sample. **b** 30° sample. **c** 60° sample. **d** 90° sample

Table 4 Characteristic stress levels obtained by DEM simulation

Angle (°)	σ_{ci} (MPa)	σ_{cd} (MPa)	σ_p (MPa)	σ_{ci}/σ_p	σ_{cd}/σ_p
0	30.4	69.1	72.4	0.420	0.955
15	27.6	76.7	78.2	0.353	0.981
30	22.4	70.0	75.7	0.296	0.925
45	30.0	73.8	79.6	0.377	0.927
60	29.2	79.2	90.2	0.324	0.878
75	43.0	95.0	101.5	0.424	0.936
90	72.7	102.8	111.0	0.655	0.926

σ_{ci} , σ_{cd} , and σ_p represent crack initiation stress, crack damage stress, and peak strength, respectively. σ_{ci}/σ_p and σ_{cd}/σ_p are crack initiation stress and damage stress normalized by peak strength

ratio method, the crack initiation stress is determined when the number of microcracks accounts for 1% of total microcracks (Jin et al. 2017). In contrast, the Poisson ratio method has concrete physical significance

and less subjectivity (Diederichs et al. 2004; Diederichs 2007), which was therefore utilized in this study. As presented in Fig. 11, the crack initiation stress is regarded as the axial stress level where Poisson ratio increases from the stage of plateau, and the corresponding values of 0°, 30°, 60°, and 90° samples are 30.4 MPa, 22.4 MPa, 29.2 MPa, and 72.7 MPa, respectively. As for crack damage stress, the ASM adopted in experiments was also utilized in DEM simulations, and the crack damage stresses of 0°, 30°, 60°, and 90° samples are 69.1 MPa, 70.0 MPa, 79.2 MPa, and 102.8 MPa, respectively (Fig. 11).

Based on above methods, the detailed characteristic stress levels of DEM models with different inclination angles are shown in Table 4, and their variation tendencies with regard to inclination angle are presented in Fig. 12. As the inclination angle increases, the crack initiation, damage stresses, and normalized crack initiation stress generally become larger, which has good

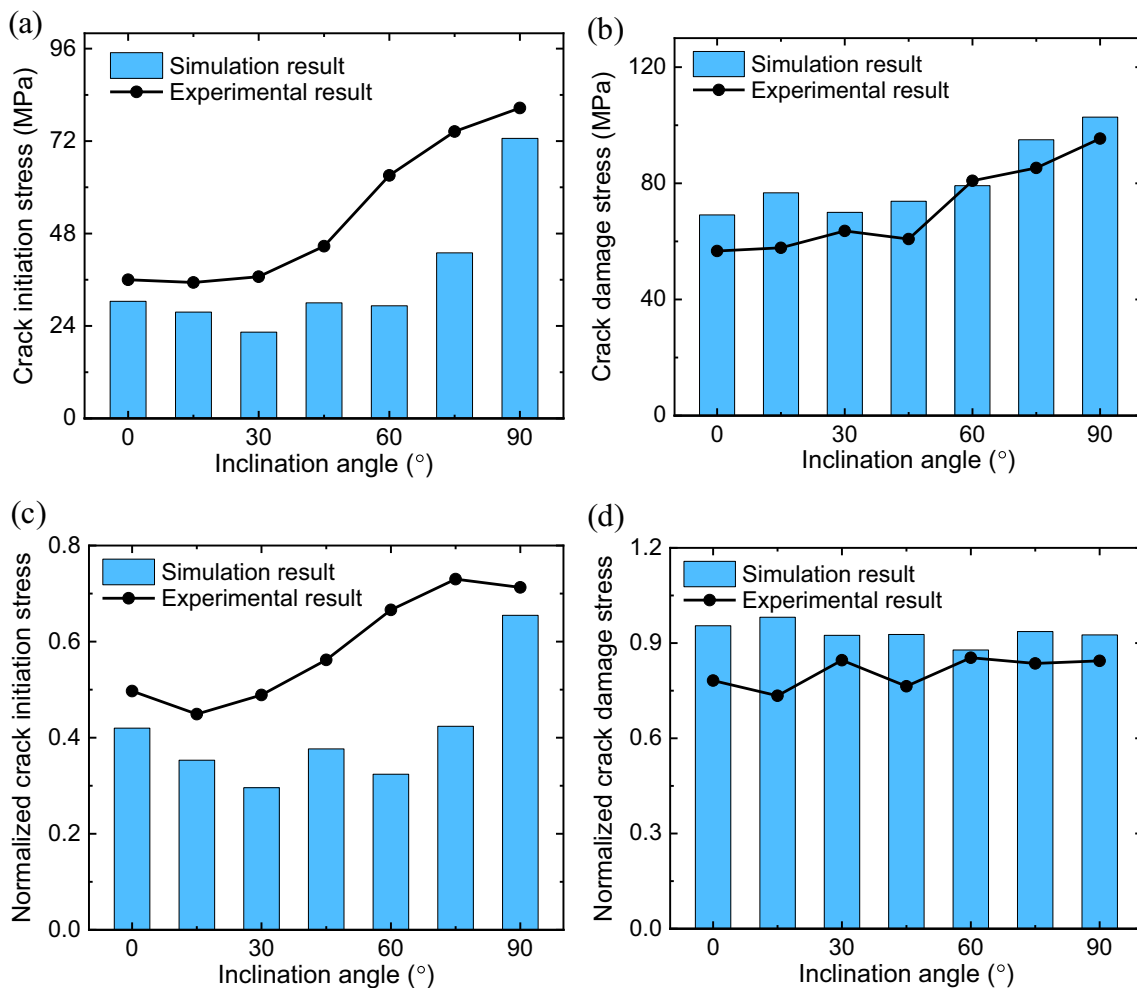


Fig. 12 Characteristic stresses and normalized characteristic stresses obtained by DEM simulation with respect to inclination angle. **a** Crack initiation stress. **b** Crack damage stress. **c** Normalized crack initiation stress. **d** Normalized crack damage stress

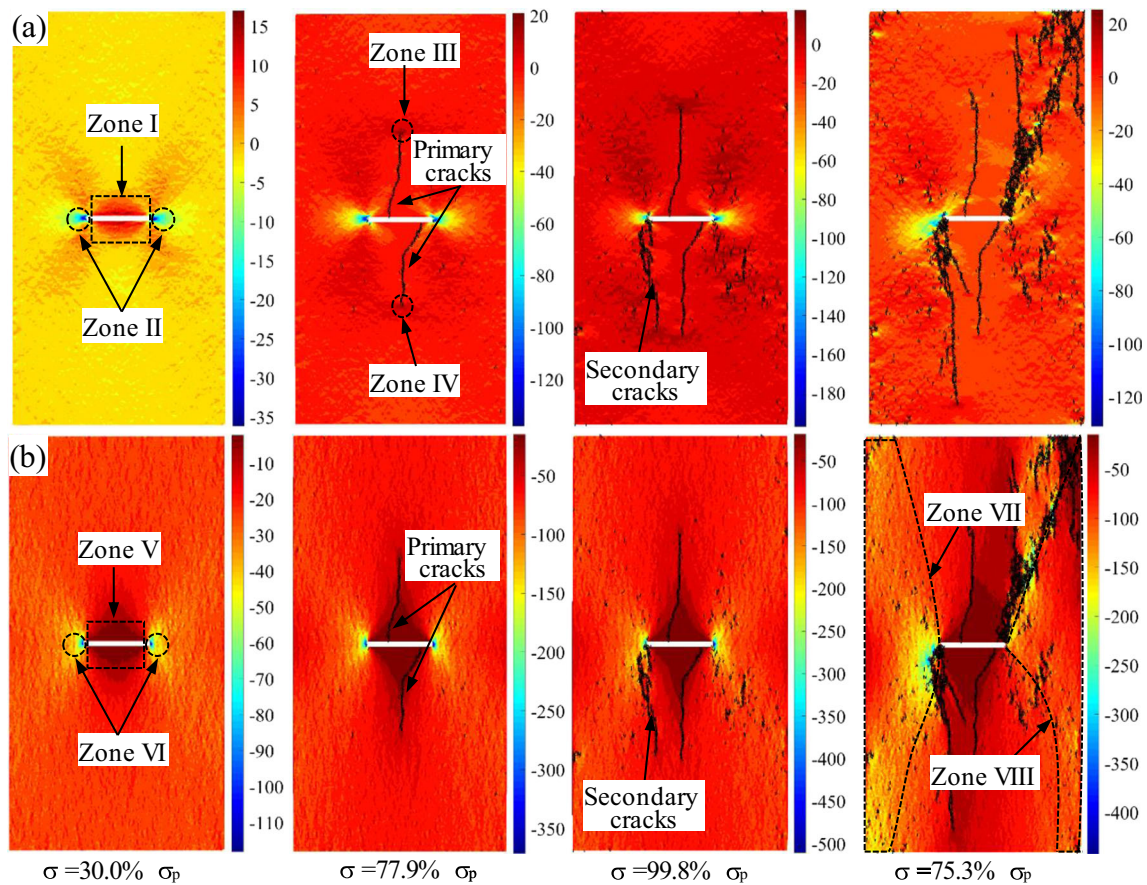


Fig. 13 Stress evolution of 0° sample under uniaxial compression. **a** Stress evolution in x direction. **b** Stress evolution in y direction. (The unit of stress in legend is MPa; the positive value represents tensile stress and vice versa)

consistence with the experimental results (Fig. 12a–c). However, the crack initiation stresses obtained by DEM simulations are lower than experimental results, which may be caused by the reason that the determination methods for crack initiation stresses in simulation and experiments are different. In terms of normalized crack damage stress, the increase of inclination angle has little influence on them, which is similar with the experimental results (Fig. 12d). Comparatively, the normalized crack damage stress obtained by DEM simulation is higher than experimental results, which is consistent with the simulation results obtained by using conventional volumetric strain reversal method (Jin et al. 2017); thus, the corresponding discrepancies may be caused by intrinsic properties of DEM simulation. Generally speaking, even though the crack initiation stress and normalized crack damage stress have slight difference between simulation and experiment, the variation tendencies of characteristic stress levels obtained by DEM simulation agree well with the experimental results, which can to some extent demonstrate that the variations of characteristic stress levels obtained by experiments are valid.

Full-field stress evolution

According to the experimental results, the full-field strain evolution of pre-cracked samples are different with regard to inclination angle. Though the strain localization phenomenon is hard to be modeled in DEM simulation, the stress evolution as the microcracks initiate and propagate can be obtained for comparison. The data of full-field stress was exported every 2000 steps during simulation, and the processes of stress evolution of 0° sample is presented in Fig. 13. Before microcracks initiate, the tensile stress along x direction concentrates in the center of pre-existing flaw (i.e., zone I in Fig. 13a), and the compressive stress along y direction is smaller than other zones (i.e., zone V in Fig. 13b), which induces the upper and bottom surfaces of pre-existing flaw deform to each other. When the deformation of upper and bottom surfaces of pre-existing flaw increases to some extent, the primary cracks initiate from the flaw center and the locations of tensile stress concentration change together with the crack tips, namely zones III and IV in Fig. 13a. In addition, with the increase of axial stress, the primary cracks are hard to propagate and the secondary cracks initiate from flaw tips,

which are consistent with the results of full-field strain evolution (Figs. 6a and 8a). Finally, when the sample approaches failure, the compressive stress among lateral regions (zones VII and VIII) is larger than other places, indicating these regions can still resist axial loading.

Figure 14 is the distribution of full-field stress in x direction. Due to the existence of pre-existing flaw, the zones of tensile stress and compressive stress have different distributions. In the cases of samples with small inclination angle, the tensile stresses are mainly concentrated around the center of pre-existing flaw (zone I), and the compressive stresses are mainly concentrated around the flaw tips (zone II). As the inclination angle becomes larger, the locations of tensile stress move towards flaw tips and were convergent with compressive stress zones when inclination angle approaches 90° , which agree well with the results of full-field strain evolution illustrated in Fig. 8c. In addition, when the samples are approximately

subjected to same axial stress ($\sim 30\%$), the stress levels in zones I and II generally decrease as the inclination angle increases, and the full-field stress distribution of 90° sample has no obvious differences with intact sample. On the other hand, the distribution of full-field stress in y direction has similar variation law. As illustrated in Fig. 15, the compressive stress concentrates around the flaw tips (zone V), while the values of compressive stress (zone IV) around the center of pre-existing flaw are smaller than other zones. As the inclination angle increases, the locations of zone IV move towards flaw tips and the stress levels generally decrease. Based on the above analysis, the pre-existing flaws with large inclination angle have little impact on the distribution of full-field stresses, which is the reason why mechanical properties especially characteristic stress levels of pre-cracked samples increase with respect to inclination angle.

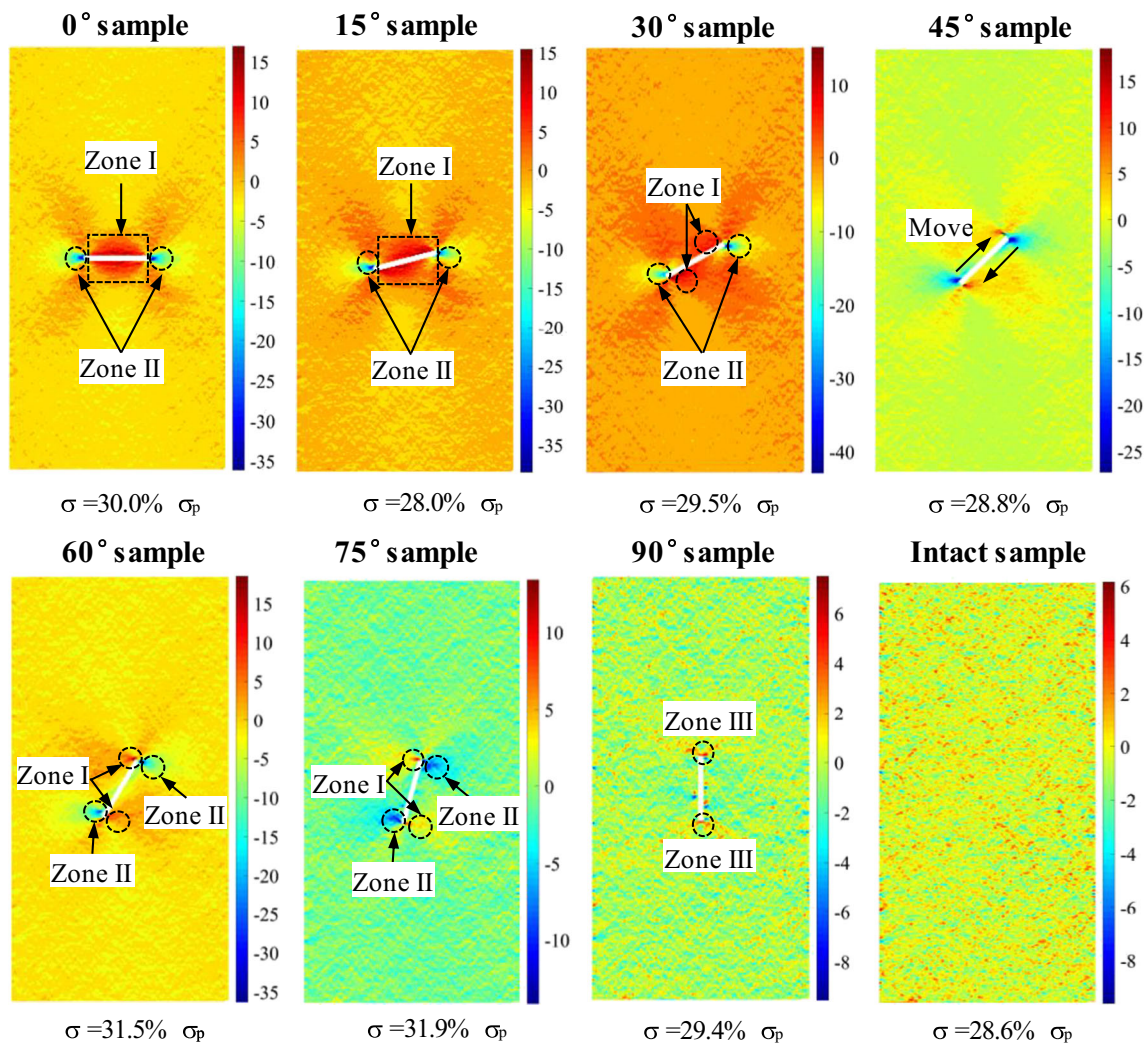


Fig. 14 Distributions of full-field stresses in x direction with respect to inclination angle (the unit of stress in legend is MPa; the positive value represents tensile stress and vice versa)

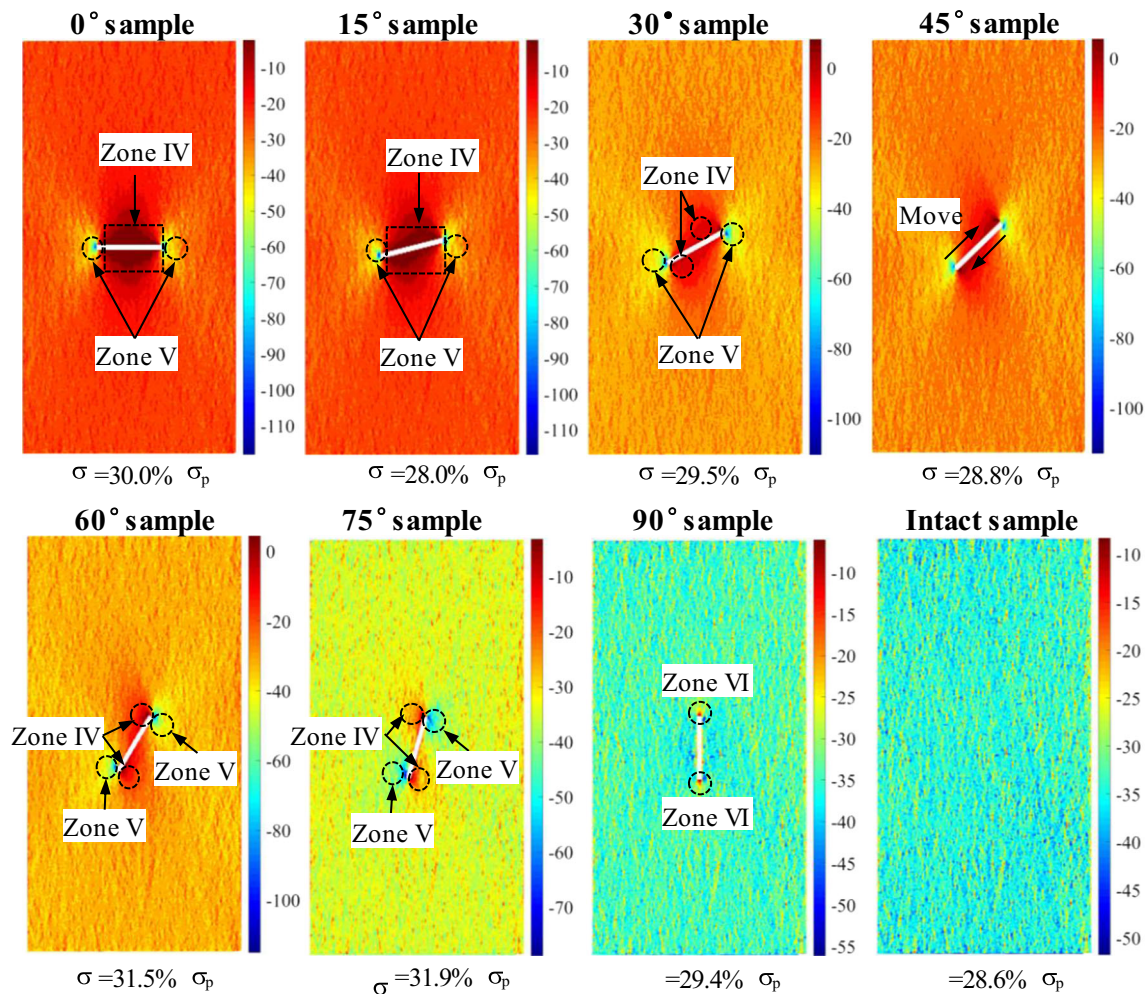


Fig. 15 Distribution of full-field stresses in y direction with respect to inclination angle (the unit of stress in legend is MPa; the positive value represents tensile stress and vice versa)

Conclusions

In this study, the uniaxial compression tests of pre-cracked marble were carried out, and the full-field strain evolution was obtained by utilizing the digital image correlation method. The variations of characteristic stress levels with respect to inclination angle are related to the distributions of full-field strain. In order to verify the experimental results, DEM was adopted for simulation and the full-field stress evolution was obtained for comparison; the main conclusions are shown below.

- (1) Pre-existing flaws can degrade the mechanical properties of rock materials, including peak strength, crack initiation, and damage stresses. When the inclination angle is small, the variations of mechanical properties are inconspicuous. As the inclination angle increases, the mechanical properties increase obviously.
- (2) According to experimental results, the normalized crack initiation stress generally increases as the inclination angle increases, while the normalized crack damage stress

- fluctuates around a constant (~ 0.8), which are consistent with the results obtained by DEM simulations.
- (3) The strain localization zones formed later can suppress the evolution of strain localization zones formed previously. When the strain localization zones firstly occur around the flaw, the axial stress level at this moment increases with regard to inclination angle, which is the reason why characteristic stress levels increase.
- (4) Around the pre-existing flaw, the tensile stress in x direction is concentrated and the compressive stress in y direction is lower than other zones. When the axial stress applied to samples is approximately same, the values of these stresses decrease as the inclination angle increases, indicating the flaws with large inclination angle have less influence on full-field stress distribution and induce the increase of characteristic stress levels.

Acknowledgments The constructive and helpful suggestions from anonymous reviewers are sincerely acknowledged. In addition, the first author would like to thank Dr. Jun Zhou from Wuhan Institute of Rock and Soil Mechanics for his assistance during experiments.

Funding information This work is supported by the National Natural Science Foundation of China (nos. 51439008, 51809137, and 41525009).

Compliance with ethical standards

Conflict of interest The authors declare that they have no conflict of interest.

References

- Amann F, Ündül Ö, Kaiser PK (2014) Crack initiation and crack propagation in heterogeneous sulfate-rich clay rocks. *Rock Mech Rock Eng* 47:1849–1865. <https://doi.org/10.1007/s00603-013-0495-3>
- Bieniawski ZT (1967) Mechanism of brittle fracture of rock. *Int J Rock Mech Min Sci Geomech Abstr* 4:407–423. [https://doi.org/10.1016/0148-9062\(67\)90031-9](https://doi.org/10.1016/0148-9062(67)90031-9)
- Blaber J, Adair B, Antoniou A (2015) Ncorr: open-source 2D digital image correlation Matlab software. *Exp Mech* 55:1105–1122. <https://doi.org/10.1007/s11340-015-0009-1>
- Bobet A (2000) The initiation of secondary cracks in compression. *Eng Fract Mech* 66:187–219. [https://doi.org/10.1016/S0013-7944\(00\)00009-6](https://doi.org/10.1016/S0013-7944(00)00009-6)
- Bobet A, Einstein HH (1998) Fracture coalescence in rock-type materials under uniaxial and biaxial compression. *Int J Rock Mech Min Sci* 35:863–888. [https://doi.org/10.1016/S0148-9062\(98\)00005-9](https://doi.org/10.1016/S0148-9062(98)00005-9)
- Brace WF, Paulding BW, Scholz C (1966) Dilatancy in the fracture of crystalline rocks. *J Geophys Res* 71:3939–3953. <https://doi.org/10.1029/jz071i016p03939>
- Brideau MA, Yan M, Stead D (2009) The role of tectonic damage and brittle rock fracture in the development of large rock slope failures. *Geomorphology* 103:30–49. <https://doi.org/10.1016/j.geomorph.2008.04.010>
- Cheng Y, Wong LNY, Zou C (2015) Experimental study on the formation of faults from en-echelon fractures in Carrara marble. *Eng Geol* 195:312–326. <https://doi.org/10.1016/j.enggeo.2015.06.004>
- Cho N, Martin CD, Sego DC (2007) A clumped particle model for rock. *Int J Rock Mech Min Sci* 44:997–1010. <https://doi.org/10.1016/j.ijmms.2007.02.002>
- Cundall PA, Strack ODL (1979) A discrete numerical model for granular assemblies. *Geotechnique* 29:47–65. <https://doi.org/10.1680/geot.1979.29.1.47>
- Diederichs MS (2007) The 2003 Canadian geotechnical colloquium: mechanistic interpretation and practical application of damage and spalling prediction criteria for deep tunnelling. *Can Geotech J* 44:1082–1116. <https://doi.org/10.1139/T07-033>
- Diederichs MS, Kaiser PK, Eberhardt E (2004) Damage initiation and propagation in hard rock during tunnelling and the influence of near-face stress rotation. *Int J Rock Mech Min Sci* 41:785–812. <https://doi.org/10.1016/j.ijmms.2004.02.003>
- Eberhardt E, Stead D, Stimpson B, Read RS (1998) Identifying crack initiation and propagation thresholds in brittle rock. *Can Geotech J* 35:222–233. <https://doi.org/10.1139/t97-091>
- Esterhuizen GS, Dolinar DR, Ellenberger JL (2011) Pillar strength in underground stone mines in the United States. *Int J Rock Mech Min Sci* 48:42–50. <https://doi.org/10.1016/j.ijmms.2010.06.003>
- Feng XT, Ding W, Zhang D (2009) Multi-crack interaction in limestone subject to stress and flow of chemical solutions. *Int J Rock Mech Min Sci* 46:159–171. <https://doi.org/10.1016/j.ijmms.2008.08.001>
- Feng P, Dai F, Liu Y et al (2018) Effects of strain rate on the mechanical and fracturing behaviors of rock-like specimens containing two unparallel fissures under uniaxial compression. *Soil Dyn Earthq Eng* 110:195–211. <https://doi.org/10.1016/j.soildyn.2018.03.026>
- Horii H, Nemat-Nasser S (1985) Compression-induced microcrack growth in brittle solids: axial splitting and shear failure. *J Geophys Res* 90:3105. <https://doi.org/10.1029/jb090ib04p03105>
- Jin J, Cao P, Chen Y et al (2017) Influence of single flaw on the failure process and energy mechanics of rock-like material. *Comput Geotech* 86:150–162. <https://doi.org/10.1016/j.compgeo.2017.01.011>
- Kranz RL (1979) Crack growth and development during creep of Barre granite. *Int J Rock Mech Min Sci* 16:23–35. [https://doi.org/10.1016/0148-9062\(79\)90772-1](https://doi.org/10.1016/0148-9062(79)90772-1)
- Lee H, Jeon S (2011) An experimental and numerical study of fracture coalescence in pre-cracked specimens under uniaxial compression. *Int J Solids Struct* 48:979–999. <https://doi.org/10.1016/j.ijsolstr.2010.12.001>
- Lee J, Ha YD, Hong JW (2017) Crack coalescence morphology in rock-like material under compression. *Int J Fract* 203:211–236. <https://doi.org/10.1007/s10704-016-0138-2>
- Li YP, Chen LZ, Wang YH (2005) Experimental research on pre-cracked marble under compression. *Int J Solids Struct* 42:2505–2516. <https://doi.org/10.1016/j.ijsolstr.2004.09.033>
- Li XF, Li HB, Liu YQ et al (2016) Numerical simulation of rock fragmentation mechanisms subject to wedge penetration for TBMs. *Tunn Undergr Sp Technol* 53:96–108. <https://doi.org/10.1016/j.tust.2015.12.010>
- Li XF, Li HB, Zhang QB, Zhao J (2018a) Dynamic tensile behaviours of heterogeneous rocks: the grain scale fracturing characteristics on strength and fragmentation. *Int J Impact Eng* 118:98–118. <https://doi.org/10.1016/j.ijimpeng.2018.04.006>
- Li XF, Li HB, Zhang QB, Zhao J (2018b) Research on the dynamic behaviour of rock material: rate dependency and pulverization. *Rock Dyn Exp Theor Appl - Proc 3rd Int Conf Rock Dyn Appl ROCODYN-3 2018* 265–270
- Li XF, Li HB, Zhao J (2019) The role of transgranular capability in grain-based modelling of crystalline rocks. *Comput Geotech* 110:161–183. <https://doi.org/10.1016/j.compgeo.2019.02.018>
- Li XF, Li HB, Liu LW et al (2020) Investigating the crack initiation and propagation mechanism in brittle rocks using grain-based finite-discrete element method. *Int J Rock Mech Min Sci* 127:104219. <https://doi.org/10.1016/j.ijmms.2020.104219>
- Lin H, Yang H, Wang Y et al (2019) Determination of the stress field and crack initiation angle of an open flaw tip under uniaxial compression. *Theor Appl Fract Mech* 104:102358. <https://doi.org/10.1016/j.tafmec.2019.102358>
- Liu T, Lin B, Zou Q et al (2015) Investigation on mechanical properties and damage evolution of coal after hydraulic slotting. *J Nat Gas Sci Eng* 24:489–499. <https://doi.org/10.1016/j.jngse.2015.04.016>
- Liu T, Lin B, Zou Q et al (2016) Mechanical behaviors and failure processes of precracked specimens under uniaxial compression: a perspective from microscopic displacement patterns. *Tectonophysics* 672–673:104–120. <https://doi.org/10.1016/j.tecto.2016.01.027>
- Liu Y, Dai F, Dong L et al (2018) Experimental investigation on the fatigue mechanical properties of intermittently jointed rock models under cyclic uniaxial compression with different loading parameters. *Rock Mech Rock Eng* 51:47–68. <https://doi.org/10.1007/s00603-017-1327-7>
- Martin CD, Chandler NA (1994) The progressive fracture of Lac du Bonnet granite. *Int J Rock Mech Min Sci* 31:643–659. [https://doi.org/10.1016/0148-9062\(94\)90005-1](https://doi.org/10.1016/0148-9062(94)90005-1)
- Miao S, Pan PZ, Wu Z et al (2018) Fracture analysis of sandstone with a single filled flaw under uniaxial compression. *Eng Fract Mech* 204:319–343. <https://doi.org/10.1016/j.engfracmech.2018.10.009>
- Moradian Z, Einstein HH, Ballivy G (2016) Detection of cracking levels in brittle rocks by parametric analysis of the acoustic emission signals. *Rock Mech Rock Eng* 49:785–800. <https://doi.org/10.1007/s00603-015-0775-1>

- Nemat-Nasser S, Horii H (1982) Compression-induced nonplanar crack extension with application to splitting, exfoliation, and rockburst. *J Geophys Res* 87:6805–6821. <https://doi.org/10.1029/JB087iB08p06805>
- Nicksiar M, Martin CD (2012) Evaluation of methods for determining crack initiation in compression tests on low-porosity rocks. *Rock Mech Rock Eng* 45:607–617. <https://doi.org/10.1007/s00603-012-0221-6>
- Pan B, Qian K, Xie H, Asundi A (2009) Two-dimensional digital image correlation for in-plane displacement and strain measurement: a review. *Meas Sci Technol* 20. <https://doi.org/10.1088/0957-0233/20/6/062001>
- Park CH, Bobet A (2010) Crack initiation, propagation and coalescence from frictional flaws in uniaxial compression. *Eng Fract Mech* 77:2727–2748. <https://doi.org/10.1016/j.engfracmech.2010.06.027>
- Potyondy DO, Cundall PA (2004) A bonded-particle model for rock. *Int J Rock Mech Min Sci* 41:1329–1364. <https://doi.org/10.1016/j.ijmms.2004.09.011>
- Sagong M, Bobet A (2002) Coalescence of multiple flaws in a rock-model material in uniaxial compression. *Int J Rock Mech Min Sci* 39:229–241. [https://doi.org/10.1016/S1365-1609\(02\)00027-8](https://doi.org/10.1016/S1365-1609(02)00027-8)
- Tapponnier P, Brace WF (1976) Development of stress-induced microcracks in Westerly granite. *Int J Rock Mech Min Sci*. [https://doi.org/10.1016/0148-9062\(76\)91937-9](https://doi.org/10.1016/0148-9062(76)91937-9)
- Wong LNY, Einstein H (2006) Fracturing behavior of prismatic specimens containing single flaws. *Proc 41st US Rock Mech Symp - ARMA's Golden Rocks 2006–50 Years Rock Mech*
- Wong LNY, Einstein HH (2009) Systematic evaluation of cracking behavior in specimens containing single flaws under uniaxial compression. *Int J Rock Mech Min Sci* 46:239–249. <https://doi.org/10.1016/j.ijmms.2008.03.006>
- Wu RJ, Li HB, Li XF et al (2020) Experimental study and numerical simulation on dynamic behaviour of transversely isotropic phyllite. *Int J Geomech*. [https://doi.org/10.1061/\(ASCE\)GM.1943-5622.0001737](https://doi.org/10.1061/(ASCE)GM.1943-5622.0001737)
- Yang SQ, Jing HW (2011) Strength failure and crack coalescence behavior of brittle sandstone samples containing a single fissure under uniaxial compression. *Int J Fract* 168:227–250. <https://doi.org/10.1007/s10704-010-9576-4>
- Yang SQ, Huang YH, Jing HW, Liu XR (2014) Discrete element modeling on fracture coalescence behavior of red sandstone containing two unparallel fissures under uniaxial compression. *Eng Geol* 178:28–48. <https://doi.org/10.1016/j.enggeo.2014.06.005>
- Yang SQ, Huang YH, Tian WL et al (2019) Effect of high temperature on deformation failure behavior of granite specimen containing a single fissure under uniaxial compression. *Rock Mech Rock Eng* 52:2087–2107. <https://doi.org/10.1007/s00603-018-1725-5>
- Zhang XP, Wong LNY (2012) Cracking processes in rock-like material containing a single flaw under uniaxial compression: a numerical study based on parallel bonded-particle model approach. *Rock Mech Rock Eng* 45:711–737. <https://doi.org/10.1007/s00603-011-0176-z>
- Zhang H, Fu D, Song H et al (2015) Damage and fracture investigation of three-point bending notched sandstone beams by DIC and AE techniques. *Rock Mech Rock Eng* 48:1297–1303. <https://doi.org/10.1007/s00603-014-0635-4>
- Zhang G, Li H, Xia X et al (2016) Effects of microstructure and micro parameters on macro mechanical properties and failure of rock. *Yanshilixue Yu Gongcheng Xuebao/Chinese J Rock Mech Eng* 35:1341–1352. <https://doi.org/10.13722/j.cnki.jrme.2015.1154>
- Zhang G, Li H, Wang M et al (2019a) Crack-induced acoustic emission and anisotropy variation of brittle rocks containing natural fractures. *J Geophys Eng*. <https://doi.org/10.1093/jge/gxz031>
- Zhang W, Sun Q, Zhang Y (2019b) Effects of pre-existing cracks and temperature on failure mode of granite from Eastern China. *J Struct Geol* 126:330–337. <https://doi.org/10.1016/j.jsg.2019.06.018>
- Zhang G, Li H, Wang M, Li X (2020) Crack initiation of granite under uniaxial compression tests: A comparison study. *J Rock Mech Geotech Eng* (Accepted)
- Zhao XG, Cai M, Wang J, Ma LK (2013) Damage stress and acoustic emission characteristics of the Beishan granite. *Int J Rock Mech Min Sci* 64:258–269. <https://doi.org/10.1016/j.ijmms.2013.09.003>
- Zhao XG, Cai M, Wang J et al (2015a) Objective determination of crack initiation stress of brittle rocks under compression using AE measurement. *Rock Mech Rock Eng* 48:2473–2484. <https://doi.org/10.1007/s00603-014-0703-9>
- Zhao XG, Cai M, Wang J, Li PF (2015b) Strength comparison between cylindrical and prism specimens of Beishan granite under uniaxial compression. *Int J Rock Mech Min Sci* 76:10–17. <https://doi.org/10.1016/j.ijmms.2015.02.009>
- Zhao C, Zhou Y m, Zhao C f, Bao C (2018) Cracking processes and coalescence modes in rock-like specimens with two parallel pre-existing cracks. *Rock Mech Rock Eng* 51:3377–3393. <https://doi.org/10.1007/s00603-018-1525-y>
- Zhao C, Niu J, Zhang Q et al (2019) Failure characteristics of rock-like materials with single flaws under uniaxial compression. *Bull Eng Geol Environ* 78:593–603. <https://doi.org/10.1007/s10064-018-1379-2>
- Zhuang X, Chun J, Zhu H (2014) A comparative study on unfilled and filled crack propagation for rock-like brittle material. *Theor Appl Fract Mech* 72:110–120. <https://doi.org/10.1016/j.tafmec.2014.04.004>